McRay - A Monte Carlo Model Coupled to CAD for Radiation Techniques

Gerd-Rüdiger JAENISCH, Carsten BELLON, Uladzimir SAMADURAU,
Federal Institute for Materials Research and Testing, Berlin, Germany
Mikhail ZHUKOVSKIY, Sergey PODOLIAKO,
Keldysh Institute for Applied Mathematics, Moscow, Russia

Abstract. In radiography, irradiating the object and recording the transmitted radiation gives information about the inner structure of an object. The transmitted radiation consists of a primary and a scattered component. The Monte Carlo method allows the detailed description of the physics of radiation transport. On the other hand, it is necessary to handle complex object geometries to be able to simulate realistic inspection scenarios. Standard Monte Carlo programs like the Monte Carlo n-particle transport code MCNP (Los Alamos National Laboratories) use mainly simple geometrical forms such as parallelepipeds, ellipsoids, or planes to construct complex geometries in a proprietary way. Here a model is presented that combines the Monte Carlo method with the world of CAD. Components are described as closed triangulated surfaces using STL as exchange format, which is supported by all CAD systems. The opportunities of the presented Monte Carlo simulation tool are discussed in terms of various examples and compared to MCNP.

Introduction

Efficient and reliable non-destructive evaluation techniques are necessary to ensure the safe operation of complex parts and constructions in an industrial environment. Radiography is one of the classical non-destructive testing techniques widely applied in industry. Over the years modelling became more and more important in modern NDE. It is increasingly used to optimise techniques for complex applications and to support the preparation of written procedures. Hence, computer modelling has to be able to handle all significant properties of a NDE system with sufficient accuracy. In case of radiological applications the model includes the radiation source, the interaction of radiation with material, the detection process, and the geometry of the part or the construction. As known from practice, the last can be very complex and requires a description that allows the handling of arbitrary geometries. The link between NDE models and CAD provides the ability to quantitatively evaluate complex inspection procedures. Depending on the formulated inspection problem or the influencing factors that should be accessed by modelling, an appropriate physical model has to be chosen to describe the underlying interaction mechanisms. The development in computer hardware allows the implementation of NDE measurement models that are capable to predict the signals seen in NDE inspections and that can be used to quantitatively study the effects of various parameters on those signals.

Standard RT simulators are based on analytical models exploiting the attenuation law and counting for scattered radiation by built-up factors. The primary radiation described by the attenuation law reaches the detector by travelling on a direct line from the source to the detector and forms the image of the specimen including defects. The scattered radiation reaches a point on the detector from any direction other than the primary. It is

often described by the built-up factor. The effect of built-up yields only a reduction of contrast in the image independent on local thickness variations of the part, i.e. it is non-image forming while contributing to the radiographic projection [1]. This approximation is valid only for parts with almost constant thickness, e.g. considering weld inspection. If the specimen covers a large range of material thickness (e.g. in case of casting inspection) this simplification cannot be used any more because the distribution of the scattered radiation becomes non-uniform, i.e. it is influenced by the object structure itself. In this case, the underlying physics has to be treated as an X-ray or photon transport problem. Several attempts are known to solve the photon transport problem based on a Boltzmann type equation for X-ray NDE applications such as moment approximation methods [2], solution of the integral transport equation [3], and the Monte Carlo method [4-7].

The Monte Carlo approach is capable to count for primary and secondary interaction mechanisms contributing to the image formation process like photon interactions (absorption, incoherent and coherent scattering including electron-binding effects, pair production, X-ray fluorescence) and electron interactions (electron tracing including X-Ray fluorescence and Bremsstrahlung production). It is a powerful tool to separate different influencing factors. On one hand the Monte Carlo code MCNP [8], which is used here as a reference, incorporates all interaction mechanisms contributing to the image forming process including electron interactions. On the other hand it is difficult to handle very complex parts with this code because of the implemented geometry model.

This paper gives an overview about our Monte Carlo implementation for radiation techniques. The major goal for this development is to overcome the restriction of the MCNP code regarding the handling of complex geometries and calculation expenses. The developed special Monte Carlo tracer allows calculating the photon path in CAD geometries with STL being the exchange format with industrial CAD packages. By introducing special algorithms, optimizing the code, and using parallel computing capabilities, the runtime of the Monte Carlo simulation has been reduced by several orders of magnitude compared to MCNP while obtaining results with comparable statistical significance.

Physics of Photon Transport

As described in [7] secondary interaction mechanisms like X-ray fluorescence and electron transport are neglected for radiographic applications. Accordingly, the physics treatment for the photon transport includes the photoelectric effect, coherent and Compton scattering while pair production does not occur for photon energies smaller then 1 MeV. Additionally form factors and scattering functions are used with coherent and incoherent scattering to count for electron binding effects.

The stationary Bolzmann equation (1) is used to model the photon transport

$$\boldsymbol{\Omega}\cdot\nabla I\left(\boldsymbol{r},E,\boldsymbol{\Omega}\right)+\mu\left(E\right)I\left(\boldsymbol{r},E,\boldsymbol{\Omega}\right)=\int_0^\infty \mathrm{d}E'\int_{4\pi}\mathrm{d}\Omega'\;\sigma\left(E'\rightarrow E,\boldsymbol{\Omega}'\rightarrow\boldsymbol{\Omega}\right)I\left(\boldsymbol{r},E',\boldsymbol{\Omega}'\right). \qquad (1)$$

It describes the variation of the photon flux $I(\boldsymbol{r},E,\boldsymbol{\Omega})$ at position $\boldsymbol{r}$ with direction $\boldsymbol{\Omega}$ and energy E. The left hand side of Eq. (1) counts for the reduction of the flux by the interaction of photons with matter given by the linear attenuation coefficient $\mu(E)$ while the right hand side describes the increase of the photon flux $I(\boldsymbol{r},E,\boldsymbol{\Omega})$ by scattering contributions from other energies E' and other directions $\boldsymbol{\Omega}'$ given by the scattering cross section $\sigma(E'\rightarrow E\,,\boldsymbol{\Omega}'\rightarrow\boldsymbol{\Omega})$. Internal photon sources such as X-ray fluorescence or Bremsstrahlung are neglected here.

The photoelectric effect consists of the absorption of the incident photon with energy E neglecting secondary effects. The absorption cross section is given by τ.

The incoherent or Compton scattering results in a changed photon flight path direction $\mathbf{\Omega}'$ given the scattering angle θ and a reduced photon energy E'. The differential Compton scattering cross section is obtained from a combination of the Klein-Nishina cross section σ_{KN} and non-relativistic Hartree-Fock incoherent scattering functions $I(Z,E,\theta)$ [9] counting for electron binding effects

$$\sigma_{Compton} = I\left(Z,E,\theta\right)\cdot\sigma_{KN}\,. \tag{2}$$

The coherent or Rayleigh scattering involves no energy loss upon scattering by an atom. Only the photon flight path direction $\mathbf{\Omega}'$ given the scattering angle θ is changed. The Rayleigh scattering cross section is obtained from a combination of the Thompson cross section $\sigma_{Thomson}$ and relativistic Hartree-Fock atomic form factors $C(Z,E,\theta)$ [10] counting for electron binding effects

$$\sigma_{Rayleigh} = C^2\left(Z,E,\theta\right)\cdot\sigma_{Thomson} \tag{3}$$

with the Thomson formula giving the scattering cross section for a free electron $\sigma_{Thomson} = \sigma_{KN}(E=0)$.

The effect of the incoherent scattering function $I(Z,E,\theta)$ and the coherent atomic form factor $C(Z,E,\theta)$ is illustrated in Fig. 1. Electron binding effects decrease the Klein Nishina cross section in forward direction (see Fig. 1, left) while the Thompson cross section is strongly forward orientated (see Fig. 1, right). The forward orientation of Rayleigh scattering increases with the photon energy. It contributes only within a very small angle range to the image in radiographic applications.

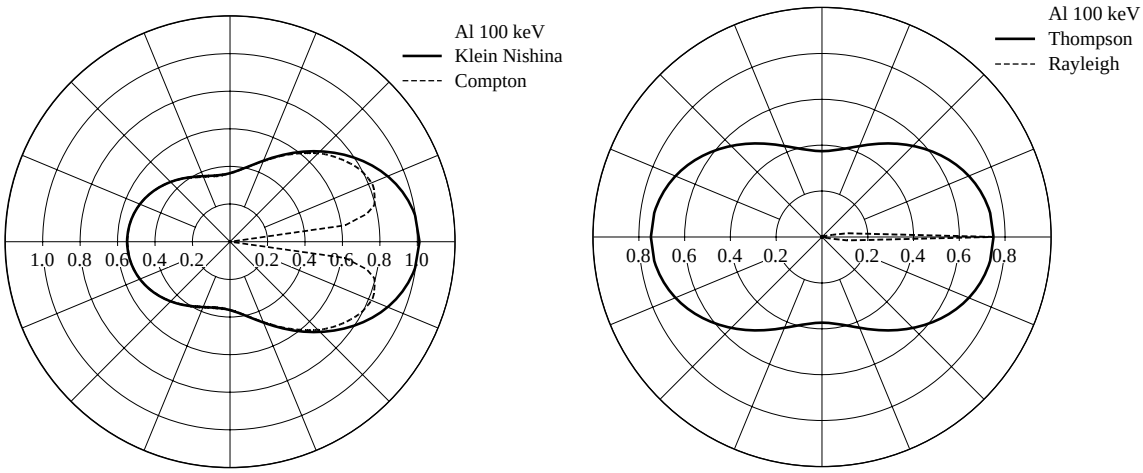

Figure 1. Comparison of Klein Nishina and Compton scattering cross section (left), and Thomson and Rayleigh scattering cross section (right) for Aluminum at photon energies of 100 keV.

2. Monte Carlo Ray Tracer Coupled to CAD Object Description

The transport scheme including variance reduction methods described in [7] is illustrated in Fig. 2 consisting of three elements: determination of the initial condition (E_0,$\mathbf{\Omega}_0$), the loca-

tion of interaction from collision length l, and the collision event $e_i(\tau, \sigma_{Compton}, \sigma_{Rayleigh})$. If the photon leaves the object no more interaction events are considered and the realization is terminated after registration in a detector element if hit. In case of an absorption event the realization is likewise finished. For a scattering event follows the determination of the new flight path direction and a possible energy loss $(E,\mathbf{\Omega}) \rightarrow (E',\mathbf{\Omega}')$, and the scheme will be repeated for the same realization from the second step. The scheme is repeated until the preset number of realizations is traced or the required statistical accuracy is reached.

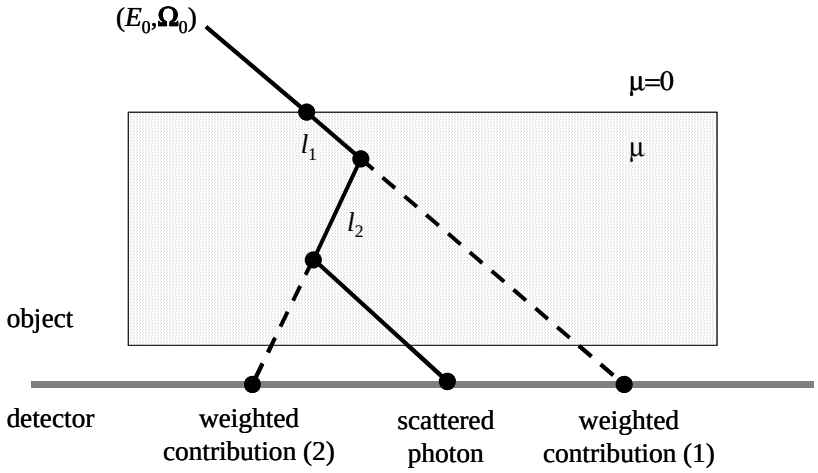

Figure 2. Monte Carlo tracing of single photon flight path: Dashed lines extend the path sections to the detector to count a weighted portion of the photon for variance reduction.

In addition to the model of radiation transport the radiographic simulation requires the virtual representation of the part or construction. Unlike other Monte Carlo codes such as MCNP, an interface to CAD has been realized. Objects are described by closed surfaces separating regions of homogeneous material properties. Several objects can be arranged in a virtual scene combined by simple Boolean operators forming complex parts. This realization also allows a flexible flaw generation and arbitrary positioning of flaws in complex parts. The surface of an object is described by plane polygons allowing a simple mathematical treatment of a single polygon or facet. The size of the polygons is given by the local surface curvature and the required accuracy of the surface approximation. The STL (stereo lithography) data format uses triangles for the boundary representation of the object. Each individual triangle description gives the xyz components for all three of the vertices and a single normal vector directed away from the object's surface. There is no order for listing the triangles specified in the STL data format, i.e. adjacent facets cannot be directly recognized. The internal data structure uses two lists extracted from the STL description: One list holds the coordinates of all vertices forming the closed surface. This reduces the data volume by avoiding multiple storage of identical vertices of adjacent facets. The second one lists all triangles forming a facet by pointing on the vertices in the first list.

The developed Monte Carlo tracer is based on the facet projection algorithms developed for our X-ray tracer described in detail in [11]. It is actually implemented in FORTRAN using MPI [12] for parallel processing. The calculations discussed below are carried out on a Beowulf cluster built from standard PC components. It consists of a 4-processor server and 37 diskless nodes holding Pentium III or Pentium 4 dual processor boards with 1 GByte memory per node. The nodes are booting the Linux kernel via network from the server.

3. Simulation Results

As discussed above, different physical models can be used to simulate the transport of photons. The following terms for describing the interaction model are used here as introduced in MCNP [8]. The simple physics treatment ignores coherent (Rayleigh) scattering and assumes incoherent (Compton) scattering on free electrons. This simplification is valid for high-energy photon problems. The full physics treatment includes coherent scattering. Additionally form factors and scattering functions are used to account for electron binging effects. Moreover, our implementation also allows counting for coherent scattering on free electrons as generalization of the simple physics model or to calculate only the incoherent scattering contribution while considering electron binding effects.

The radiographic setup used for the below discussed examples is shown in Fig 3. The source is positioned 100 cm above the center of the detector plane having an opening angle of 0.08 rad. An ideal detector is assumed of size 15 x 15 cm with 300 x 300 pixels. Profile plots discussed below refer to the central line of the detector as shown in Fig. 3.

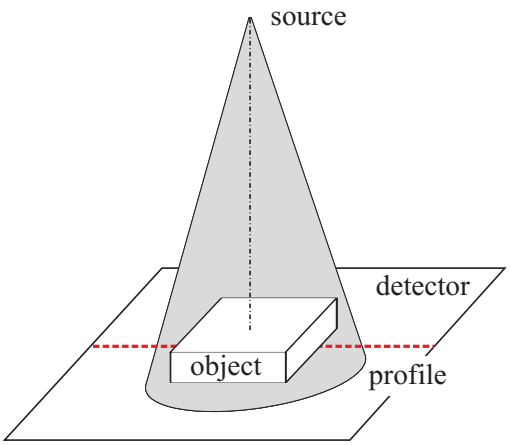

Figure 3. Radiographic setup.

3.1 Simple Part Geometry and the Contribution of Compton and Rayleigh Scattering

The contribution of scattered radiation to the image formation is discussed here for simple plate geometry. The following parameters have been chosen for the Monte Carlo calculations: monochromatic source: 100 keV, opening angle 0.08 rad, source to detector distance 100 cm, steel plate placed on detector plane: $5 \times 5 \times 1$ cm^3, ideal detector: 15×15 cm^2 (300×300 pixels).

The centreline profile for the scattered radiation are shown in Fig. 4 without counting for electron binding effects. Here the black lines give the results including electron binding effects called full physics referring to the MCNP notation. The grey lines present the scattering distributions without considering electron binding effects called simple physics. For both physical models the contribution of Rayleigh scattering (dashed lines) is studied.

Comparing the results with and without Rayleigh scattering for simple physics (gray lines), almost no difference is found directly behind the plate for positions -2.5 cm < x < 2.5 cm. This result can be explained as follows: The distribution of the scattering angle for Rayleigh scattering does not depend on the photon energy and shows a symmetric distribution with respect to the forward and the backward half space if binding effects are neglected (see Fig. 1). Additionally, the Rayleigh interaction cross section is about a factor of 3.5 smaller compared to the Compton cross section and about a factor of 5 smaller than the absorption cross section for steel at 100 keV. These facts together explain that the contribu-

tion of Rayleigh scattering is negligible directly behind the plate in this case. Furthermore an increase of the scattering contribution is found next to the edges of the plate. This effect has been discussed earlier [13]. Rayleigh scattering increases the maximum due to the scattering angle distribution.

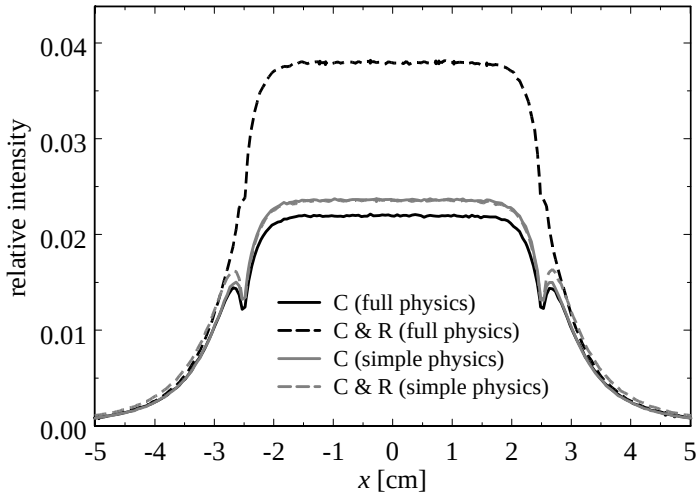

Figure 4. Comparison of scattered radiation behind 10 mm steel plate for different physical models.

Looking at the results for full physics a considerable contribution of Rayleigh scattering is found (compare the full and dashed black lines in Fig. 4). Rayleigh scattering almost doubles the scattered radiation because of the strong forward direction of the scattering angle distribution for Rayleigh scattering because of electron binding effects (see Fig. 1). The decrease of the Compton contribution behind the plate compared to the simple physics model can be drawn back to the fact that Compton scattering into the forward half space is reduced while considering binding effects. Rayleigh scattering decreases the maxima found next to the edges of the plate because of its strong forward directivity.

3.2 Complex Part Geometry

The applicability of the developed Monte Carlo model to multi-material objects and to engineered parts of complex geometry is demonstrated by three examples. The results are given in Figs. 5 through 7. Electron binding effects are neglected.

Fig. 5 shows the results for a part of $5 \times 5 \times 1$ cm^3 composed of two plates $5 \times 2.5 \times 1$ cm^3 made from steel (left) and aluminium (right). In the centre of both plates a cubic void of $0.5 \times 0.5 \times 0.5$ cm^3 was placed. The primary intensity behind the aluminium plate (right) is larger because of a smaller attenuation compared to steel. Both voids are clearly visible. The scattered image shows the same behaviour. Only the edges of the objects are blurred and the contrast is decreased. Anyway, a clear indication of the voids is found in the scattered image. A higher intensity in the void area is seen for steel while a smaller for aluminium. The scattering volume behind the void is the same in both cases, but the mean free scattering path length is considerably smaller for steel compared to aluminium increasing the chance of scattering to occur. As a result a larger scattering intensity is found behind the void compared to the surrounding area for steel. For aluminium the overall scattering intensity is larger compared to steel because aluminium is a less attenuating material. But the decrease of the scattering volume by the void considerably decreases the chance of scattering yielding a smaller contribution in the void area.

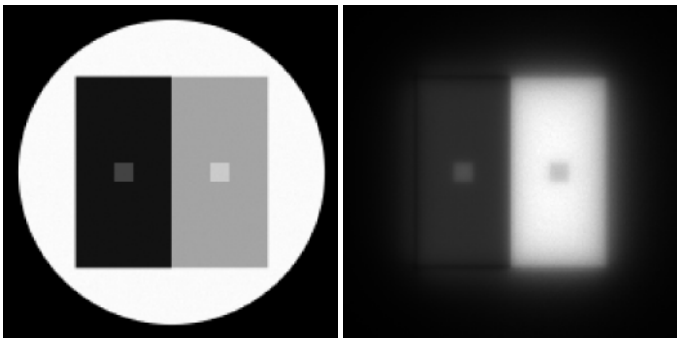

Figure 5. Multi material part: primary intensity (left), scattering intensity (right).

Figs. 6 and 7 show the results for a goblet (1128 facets) and a rotor (106759 facets) for 200 keV monochromatic X-rays. The scattering intensity for the goblet indicates higher contributions from the shaft because of increased scattering volume. The distribution for the rotor is axially symmetric because of the geometry of the rotor.

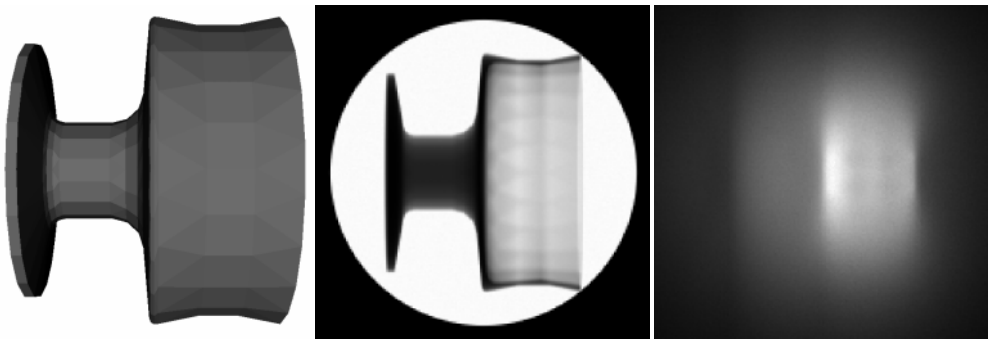

Figure 6. Goblet: part (left), primary intensity (center), scattering intensity (right).

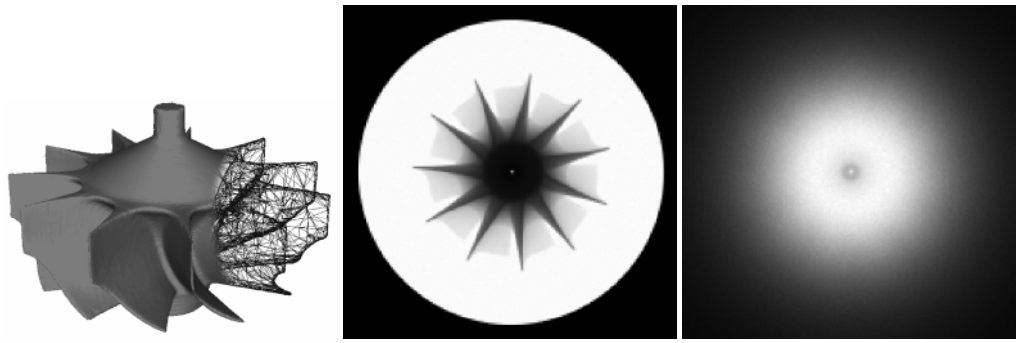

Figure 7. Rotor: part (left), primary intensity (center), scattering intensity (right).

3.3 Comparison to MCNP

A comparison with the standard Monte Carlo code MCNP was executed. For this purpose a $5 \times 5 \times 0.5$ cm^3 steel plate was irradiated by a 100 keV monochromatic X-ray point source. For comparison purposes only the first Compton scattering event is considered for simple physics treatment. The results presented in Fig. 8 show an exact agreement between the model discussed here and MCNP. It has to be pointed out that this excellent agreement has been received only if the MCNP data base for the photon interaction cross sections is used. The results, especially for the distribution of scattered radiation, are very sensitive to the cross sections used for the calculation. Small variation of the cross sections can yield disagreement with the MCNP results by several percent. Further comparisons will be executed in the future.

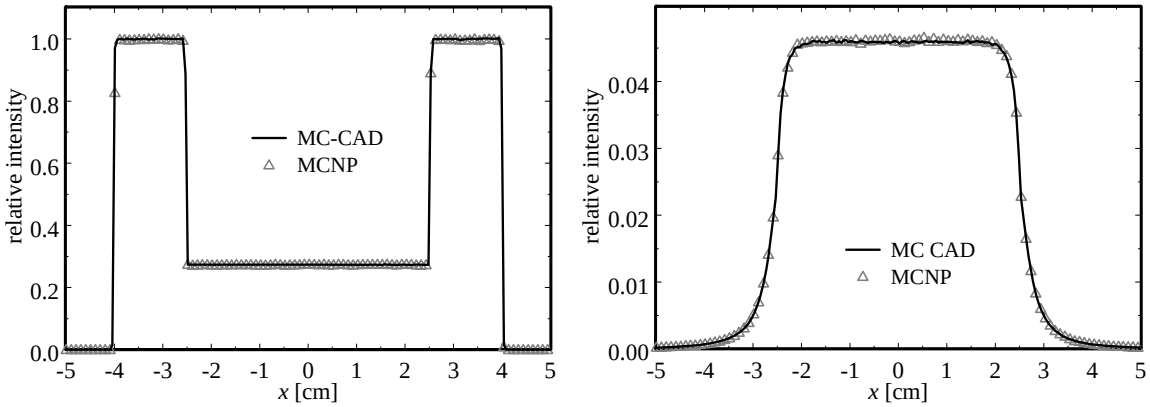

Figure 8. Comparison of primary (left) and scattered (right) radiation with MCNP results counting for the first scattering event.

4. Conclusions

State-of-the-art radiography simulators have a broad application range. These simulators are based on the attenuation law to describe the primary radiation. Monte Carlo models can be used to describe the effect of scattered radiation in detail. The discussed Monte Carlo implementation overcomes the problem of standard codes in handling complex part geometries because it couples Monte Carlo photon transport with CAD object description. The presented examples demonstrated its applicability to industrially designed parts with acceptable computing expenses. The comparison to the MCNP code shows exact agreement.

References

[1] Halmshaw, R., *Industrial Radiology*, Chapman & Hall, London, 1995

[2] Tillack, G.-R., Artemiev, V. M., and Naumov, A. O., *JNDE* **20** 4, 153 (2001)

[3] Inanc, F. and Gray, J. N., *Applied Radiation and Isotopes* **48** 10-12, 1299(1997)

[4] Bell, Z. W., in *Review of Proggress in QNDE*, Vol. 10, eds. D. O. Thompson and D. E. Chimenti, Plenum Press, New York, 1991, pp. 347-353

[5] Aerts, W., De Meester, J. R., and Bollen, R., *Mat. Eval.* **40** 9, 1071 (1982)

[6] Inanc, F., in *Review of Progress in QNDE*, Vol. 22, eds. D. O. Thompson and D. E. Chimenti, AIP, New York, 2003. pp. 545-552

[7] Zhukowsky, M., Podoliako, S., Jaenisch, G.-R., and Bellon, C., in *Review of Progress in QNDE*, Vol. 23, eds. D. O. Thompson and D. E. Chimenti, AIP, New York, 2004. pp. 515-521

[8] Briesmeister, J. F. (ed.), *MCNP–A General Monte Carlo N–Particle Transport Code*, LANL Report LA–13709–M, Los Alamos, 2000

[9] Hubbell, J. H., Veigele, W. J., Briggs, E. A., Brown, R. T., Cromer, D. T., and Howerton, R. J.: *Atomic Form Factors, Incoherent Scattering Functions, and Photon Scattering Cross Sections*. J. Phys. Chem. Ref. Data **4,** 471-538 (1975); erratum in **6,** 615-616 (1977)

[10] Hubbell, J. H. and Overbo: Relativistic Atomic Form Factors and Photon Coherent Scattering Cross Sections. J. Phys. Chem. Ref. Data **8,** 69-105, (1979)

[11] Bellon, C., *Computersimulation radiographischer Prüfverfahren*. PhD thesis, Dresden University of Technology, Logos-Verlag, Berlin, 2001

[12] *MPI: A Message-Passing Interface Standard*. University of Tennessee, Knoxville, 1994

[13] Tillack, G.-R., Artemiev, V. M., Gray, J. N., in *Review of Progress in QNDE*, Vol. 18, eds. D. O. Thompson and D. E. Chimenti, Kluver, New York, 1999, pp. 631-638